Article:
Sun, X., Yu, Y., Niu, X. et al. (2026) A dual-resolution acoustic-sensing robot for autonomous in-pipe inspection. Tunnelling and Underground Space Technology, 168, Part 1. 107133. ISSN: 0886-7798

https://doi.org/10.1016/j.tust.2025.107133

A dual-resolution acoustic-sensing robot for autonomous in-pipe inspection

Xiaoyu Sun[a,*], Yicheng Yu[b,*], Xudong Niu[a], Zhenshan Wang[a], Alexander R. K. Towlson[a], Kirill V. Horoshenkov[b], Anthony J. Croxford[a], Bruce W. Drinkwater[a]

[a]*School of Electrical, Electronic and Mechanical Engineering, University of Bristol, Queen's Building, University Walk, Bristol BS8 1TR, United Kingdom*

[b]*School of Mechanical, Aerospace and Civil Engineering, University of Sheffield, Mappin Street, Sheffield S1 3JD, United Kingdom*

Abstract

This paper presents the development of an acoustic-sensing robotic system designed for autonomous in-pipe inspection. Existing methods, such as camera-based visual sensing and laser-based distance scanning systems, offer high-resolution and rapid spatial data but are often unsuitable for long-term deployment in adverse environments. Recent developments show that acoustic sensing methods can offer power- and data-efficient inspection for long-term service. This paper explores autonomous in-pipe inspection using only acoustic measures for remote pipe monitoring. We propose a dual-resolution acoustic sensing strategy that employs low-frequency acoustic waves for long-range coarse sensing and navigation, paired with high-frequency acoustic waves for short-range, high-resolution imaging. A robotic system and corresponding data characterisation and classification method was developed based on this strategy, enabling autonomous inspection. Experimental findings show that the robot can effectively localise multiple features within the pipe setup, achieving an average localisation variation of 8 cm over a total length of 1800 cm. Additionally, the system effectively classifies features, specifically aligned pipe structures, tilted pipe structures, blockages and empty pipes, with an average accuracy of 76% during autonomous inspections.

Keywords: In-pipe inspection, Autonomous robot, Acoustic sensing, Buried pipe

1. Introduction

Fluids such as oil, gas, and water are essential materials for modern daily life and are transported through pipelines [1, 2, 3]. Pipeline infrastructure is capital-intensive and designed for long, stable service lives [4, 5]. However, much of this infrastructure, specially for water and sewer pipes, is often considered 'forgotten', and operates under risks associated with aging, corrosion, and maintenance neglect [6, 7, 8]. Given the critical role these facilities play, it is imperative to schedule regular inspections, maintenance, and repair to prevent service disruptions, which could lead to significant socioeconomic impact [9, 10]. Nevertheless, inspecting buried infrastructure poses significant challenges, and maintenance is often reactive, occurring only after a major failure. Therefore, effective strategies are necessary to inspect the internal conditions of buried pipelines with minimal service interruption [11, 12].

One popular solution for pipe inspection is in-pipe remote inspection using a mobile platform, typically referred to as in-pipe inspection robots [1, 2, 3, 13]. However, due to variations in sensing environments, the mechanical design and sensing strategies of these robots varies significantly. For example, pipe infrastructure with high fluid levels, such as water supply, oil, and rising main pipes in the sewage system, require robotic mechanisms and sensing methods adaptable to liquid-filled environments [1, 3, 13]. Conversely, pipe facilities with low fluid levels, such as gas pipes and most sewer pipes, can employ robotic mechanisms designed for open-air use, and the sensing methods should be capable of operating in air-coupled conditions [2, 9, 11]. Despite the varieties of robotic platforms available for in-pipe inspection, the majority rely on tethered platforms, requiring cables for power supply, remote control, and data transmission. Consequently, inspecting buried pipelines with these devices often results in service interruptions, increased operational costs, and time-consuming procedures due to the necessity of human intervention [14].

*Corresponding author

Email addresses: x.sun@bristol.ac.uk (Xiaoyu Sun), yicheng.yu@sheffield.ac.uk (Yicheng Yu)

The focus of this paper is on investigating autonomous sensing methods for in-pipe inspection of sewer systems with low fluid levels. Optical sensing methods, specifically the visual-based CCTV cameras, are the most popular sensing technique for this type of robotic in-pipe inspection. Various systems having been commercialised for real-world applications, such as RedZone (USA), RapidView (USA), Minicam (UK), and iPEK (Germany), offering manually controlled platforms for in-pipe inspection based on cameras [15, 16, 2, 11]. These platforms typically employ high-resolution camera modules with auxiliary lighting for inspections, supported by a tethered crawler for data transfer and remote manual operation [13]. Long-duration, high-resolution videos can be recorded, and AI-assisted video inspection algorithms are subsequently employed to detect pipe defects, such as sub-centimetre surface cracks and roots on pipe walls [17, 18, 19]. However, this technique currently requires human intervention for robot control, data acquisition and processing. Moreover, high-resolution video data requires high power computational hardware capabilities, which are limited for robotic systems designed for in-pipe applications and rely on tether-based designs. Hence, visual-based in-pipe robots remain limited for autonomous inspections despite decades of development [14].

Electromagnetic sensing is another approach for remote in-pipe inspection used on moveable platforms, including techniques such as magnetic flux leakage (MFL) inspection and eddy current (EC) techniques [20]. Various sensing apparatuses have been reported to use eddy-current-based sensing methods for surface deformation localisation [21], sub-surface detection [22] and imaging [23, 24]. The overall sensing performance shows that electromagnetic sensing based on eddy current is effective for detecting and characterising small, near-surface defects, although its application is restricted to conductive materials, which limits its use.

Acoustic sensing includes a variety of methods and devices developed for in-pipe inspections, which can be categorised into active and passive sensing techniques [25]. An example of passive acoustic sensing is the SmartBall, a spherical device produced by Pure Technologies, USA, used for in-pipe inspection [26]. Propelled by fluid flow, this device is submerged in the fluid and continuously records ambient noise to detect anomalies such as leaks, which are identifiable by distinctive acoustic responses at the leakage points. Field experiments have demonstrated that this device can detect water leakages as small as 0.8 litres per second in cast iron pipes, with localisation accuracy within 1 metre using acoustic waves within the audible range (< 20 kHz). However, the report also indicates that the acoustic sensor is less effective on plastic pipes due to the high acoustic attenuation properties of the material [26].

Active acoustic sensing has been widely used for in-pipe inspections. Integrated systems, such as Kurt [27], Makro [28], Telerobot [29], Tetrix [30], and Lego-EV3 [31], all employ ultrasonic distance sensors (UDSs) as part of their sensing capabilities. UDS, a type of air-coupled active acoustic transducer, transmits and receives ultrasonic pulses (typically operated around 40 kHz) to detect obstacles. This low-cost, compact sensor provides time-of-flight (ToF) data of the nearest object, which, while adequate for feature detection, is limited in characterisation capabilities [32]. Recent developments in active acoustic sensing have shifted focus towards acoustic scanning and imaging, utilising array transducers on movable pipeline inspection gauges (PIGs). Zhong et al. reported a robotic innovation integrating ultrasonic phased arrays on a wheeled continuum robot for conducting in-pipe ultrasonic C-scans — a 2D spatial scanning strategy [33]. The system utilises four 128-element linear convex phased arrays to form a circumferential array matched to the pipe's inner diameter, enabling C-scans within metallic pipes at 5 MHz. Experimental results demonstrated that this system can detect flat-bottom hole defects as small as 3 mm in diameter on the pipe's outer surface. Rachev et al. described an in-pipe inspection using PIG-mounted ultrasonic phased arrays (5 MHz) for imaging crack-type defects [34]. Using plane wave imaging (PWI) [35] and the total focusing method (TFM) [36], the experiments showed that these imaging algorithms could quantitatively characterize changes in crack length based on the imaging results. Vithanage et al. developed an ultrasonic phased array roller probe for automated in-process welding inspection of pipe structures [37]. Operating at 5 MHz, this linear phased array is housed within a water-filled rubber roller, performing ultrasonic imaging using angled transverse bulk waves to enhance the detection of defects with varied orientations. Notably, this development is intended for external pipe welding inspections, but the concept—based on angled ultrasonic phased arrays and a rolling system—could be adapted for in-pipe inspections.

Overall, high-frequency (MHz) ultrasonic sensing produce high-resolution, user-friendly image results for quantitative defect inspection but cannot be used for robotic navigation due to limited sensing range and coupling conditions. In contrast, airborne low-frequency acoustic sensing (≤ 40 kHz) can provide distance information for robotic navigation with a long ranging cover-

age and signal simplicity, desirable features for the autonomous in-pipe sensing development. However, due to the low operating frequencies, current implementations of these sensing measures lack accuracy, which makes them limited for quantitative inspection for structural objects.

This paper presents the development of a robotic apparatus for autonomous in-pipe inspection based on acoustic sensing methods. To facilitate untethered autonomous operation, a dual-resolution, air-coupled, active acoustic sensing method is employed. One sensing resolution is metre-scale using low-frequency acoustic waves at Hz levels, ideal for scoping pipe features over long distances (> 2 m) [38]. The other sensing resolution is centimetre-scale using a narrow-band 40 kHz ultrasonic wave, which is commonly used in air-coupled UDS applications [39]. An air-coupled ultrasonic array developed with 40 kHz acoustic transducers enables high-resolution imaging within approximately 1 m [40, 41]. By integrating these two frequency ranges, the proposed robotic apparatus can autonomously perform in-pipe inspections with relatively simple signals, i.e. acoustics at different resolutions, eliminating the need for a tethered system for power, data communication, or remote human control.

A portable ultrasonic array data acquisition device is developed for ultrasonic array sensing on a robot. A dynamic ultrasonic image binarisation and an image classification strategy are proposed for autonomous in-pipe inspections based on ultrasonic images. The experimental results show that the developed robot can perform autonomous in-pipe inspection with good feature classification performance. This paper is structured into seven sections. Section 2 details the hardware components of the developed robot. Section 3 describes the sensing methods, covering both low-frequency acoustic sensing and high-frequency ultrasonic imaging for in-pipe inspections. Section 4 discusses the development of pipe feature classification approaches based on ultrasonic images. Section 5 outlines the design of the sensing logic for autonomous in-pipe inspection. Finally, Section 6 demonstrates the performance obtained from a laboratory-level experiment on an autonomous in-pipe network inspection.

2. Hardware

2.1. The robotic platform

Fig.1 illustrates the robotic platform developed for autonomous pipe inspection using acoustic sensing techniques. As shown in Fig.1(a) and (b), the robot is equipped with three main functional units: the control unit, the motion unit, and the sensing unit. The control unit incorporates two micro-computer components (4B, Raspberry Pi, UK), one of which is dedicated to motor control. This includes four independent PID motors (MG513X, Wheeltec, China) and a 4-channel motor driver board (D24A, Wheeltec, China). The other micro-computer is dedicated to control all sensing devices. As illustrated in Fig.1(b), the robot employs two types of acoustic sensing devices: a low-frequency acoustic sensing setup and a high-frequency ultrasonic imaging setup.

The acoustic sensing configuration includes a loudspeaker (2242, Visaton, Germany), accompanied by a six-microphone array and its controller board (Respeaker 6-mic, Seeed Studio, China). Note that this acoustic hardware selection is referred to previous work [38, 42, 43]. The ultrasonic imaging setup consists of an air-coupled ultrasonic array formed by 40 kHz transducers (MA40S4R, Murata, Japan), paired with a self-developed portable array controller. It is worth noting that the majority of the electronic components used are off-the-shelf products, with only the portable ultrasonic array controller and the air-coupled ultrasonic array being specifically developed as part of this work.

All acoustic and ultrasonic sensors are mounted on a disc-shaped sensor holder with a diameter of 120 mm, which is suitable for in-pipe deployment into UK's sewer mains with a typical diameter of 300 mm. At the centre of this holder, the loudspeaker is positioned, circled by the six-microphone array arranged on a hexagonal PCB plate with sides of 50 mm each. The 24 ultrasonic transducers are organised into 12 pairs and arranged in a clock-shaped circular array with a diameter of 110 mm. The loudspeaker and hexagonal microphone array operate in the low-frequency range, typically from 300 Hz to 600 Hz, for transmitting and receiving acoustic waves. Low-frequency acoustic waves are chosen for their ability to travel long distances with low attenuation in pipe structures, making them suitable for long-range coarse resolution sensing. The ultrasonic transducer array operates at a central frequency of 40 kHz, providing limited propagation distance (upto 1.2 m in the presented setup) but enabling high-resolution and sensitive object characterisation through ultrasonic imaging algorithms. Therefore, the robotic apparatus developed in this study performs dual-resolution acoustic sensing, offering a sensing solution with both long-range coverage and high-resolution characterisation for autonomous in-pipe inspection. Fig.1(c) shows the robotic apparatus and a sewer pipe section, which is made of polyvinyl chloride (PVC) with an inner diam-

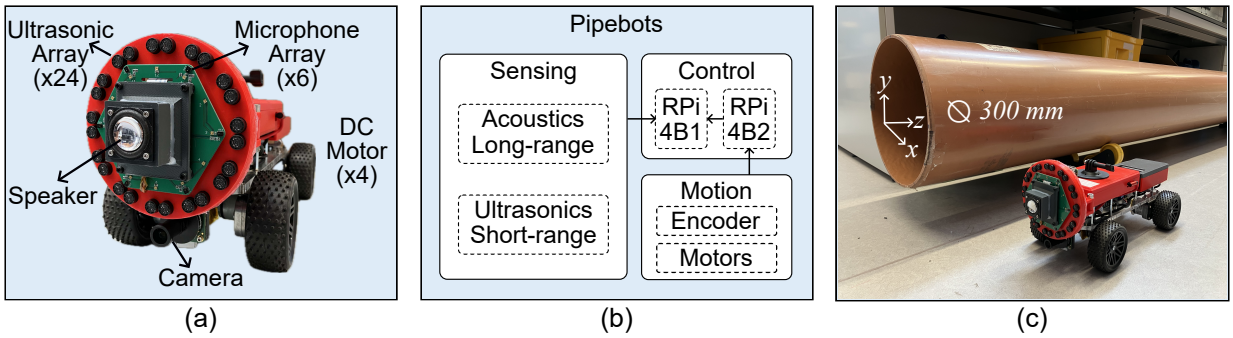

Figure 1: Diagram of the developed robotic platform, (a) illustrates the components on the robot and (b) shows the block diagram of the developed robotic platform, and (c) shows the photo of the developed robotic compared with the testing pipe section with a diameter of 300 mm. Note that testing sewer pipes used in this paper are certificated to BS EN 1401-1.

eter of 300 mm and complies with the BS EN 1401-1 standard.

2.2. A portable ultrasonic array controller

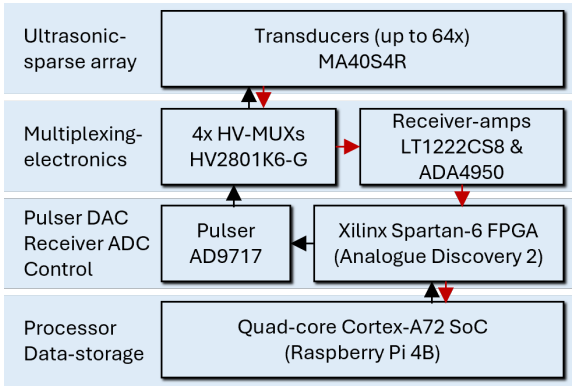

Figure 2: Diagram of the developed portable array controller for ultrasonic array data acquisition on robotic platforms. Note that this figure is the detailed description of the 'Ultrasonics' block shown in Fig.1(b). Note that black arrows indicate the signal transmission path and red arrows indicate the signal reception path.

A portable array controller has been developed for the ultrasonic array data acquisition on the robot. This was developed using an off-the-shelf single-channel ultrasonic controller (Analog Discovery 2, Digilent, USA) integrated with a 64-channel multiplexing board, facilitating array data acquisition. The overall physical size of this controller is appropriately 90 mm $\times$ 90 mm $\times$ 10 mm with a weight of 67 g. It operates on a single USB 3.0 cable, which provides both power and data transmission, consuming a maximum power of 4.5 W at a voltage of 5 V. Note that this power consumption occurs solely during the ultrasonic data acquisition process.

Fig.2 shows the electronic block diagram of the developed portable array controller. As mentioned above, a Raspberry-Pi micro-computer is used to control the array controller via a USB 3.0 port, as shown in the bottom block. The field programmable gate array (FPGA) (Xilinx Spartan-6, AMD, USA) in the array controller can then generate an ultrasonic excitation pulse via a 14-bit digital-to-analogue converter (DAC) (AD9717, Analog Devices, USA). This excitation pulse will then pass through an analogue multiplexer (HV2801, Microchip, USA) to a specific transmitting element on the array transducer to generate an ultrasonic wave. The corresponding backscattered ultrasonic signal will then be acquired by a specific receiving element and transferred to the analogue-to-digital converter (ADC) (AD9648, Analog Devices, USA) via the multiplexer. This received ultrasonic signal is amplified by a two-stage receiver amplifier made up of an operational amplifier (LT1222, Linear Technology, USA) and a differential amplifier (ADA4950-1, Analog Devices, USA). The amplified received signal is then passed to the microcomputer for storage. Using this system the time domain signals are recorded from all combinations of transmit and receive transducers in a process know as full-matrix capture (FMC) [36]. Detailed hardware design and wiring files of the developed portable multiplexing array controller can be accessed from Section S1 in the supplementary information [44].

3. A dual-resolution acoustic sensing method

3.1. Acoustic long-range scoping

According to the previous study [38], there are a number of distinct acoustic wave modes propagating in a typical duct structure (i.e. a pipe structure). Here mode$(0, 0)$ is chosen for long-range acoustic sensing, as

this plane wave mode allows non-dispersive (i.e. velocity is independent of frequency) acoustic propagation in a duct structure. The frequency limit of the (0,0) mode in a 300 mm diameter pipe structure is 675 Hz [45], which is the reason of choosing the frequency range for excitation from 300 Hz to 600 Hz. Acoustic signals collected in real-world environments normally contain noise induced by both the environment and the measurement system, which affects the signal-to-noise ratio (SNR) of the sensing result. A denoisng method, the SpaRSA algorithm [46], is implemented to reduce the noise effect by solving the sparse representation problem simplified by the basis pursuit denoising (BPDN) [47] method with a wavelet dictionary (*sym*4 wavelet function by the MATLAB function @*wmpdictionary*). The final wavelet represented acoustic signal and more detail of the methodology can be found in Section S2 or in the previous work [38, 42, 43].

Fig.3 demonstrates four example acoustic signals measured from different structural features with a straight pipe setup. Fig.3(a) shows the acoustic signal of a 4-section straight pipe structure. An echo is shown at the position corresponding to the pipe end, which is generated due to the acoustic impedance change from the internal pipe structure to the open-air environment [38]. It is worth noting that reflections produced by well-aligned joint structures are too small to resolve using the current acoustic sensing setup. Fig.3(b) shows the acoustic echo of a tilted joint, which has a tilt angle about 5° along the pipe axial direction, at 900 cm in the pipe structure. Fig.3(c) shows the acoustic echo generated from a pipe-corner. Note that there is an additional 300 cm pipe section attached after the corner section, which yields the echo at 1200 cm. This signal shows that the applied acoustic wave can propagate around pipe corners to a different direction. Fig.3(d) shows the echo from a 120 cm diameter manhole at 900 cm. This signal shows that a manhole generates long acoustic response in the time domain, which restricts detection capabilities beyond its location. However, since the robot can be accessed through the manhole, the robotic system developed in this paper is designed to enable autonomous pipe inspection between adjacent manholes.

Another point in Fig.3 is the small discrepancy between the feature echo locations (red dots marked at the echo start points) in the time domain and the actual feature locations (indicated by red dashed lines). The feature echo locations in the acoustic signals are determined by applying a thresholding approach, where the threshold is set to one-tenth of the echo amplitude of the pipe-end feature. However, those location mismatches generated from acoustic sensing (300 to 600 Hz) are

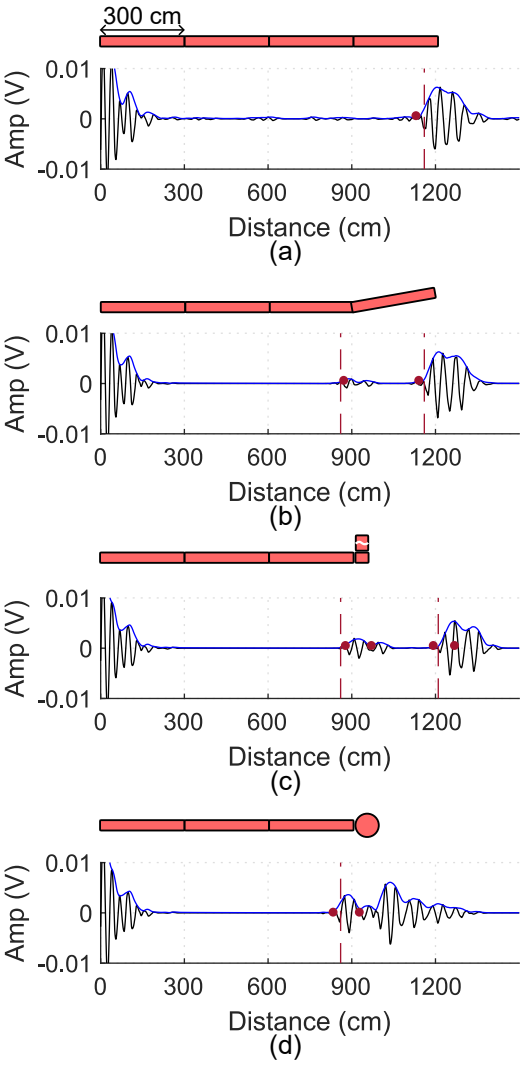

Figure 3: Acoustic signals at different pipe structures, (a) shows the acoustic signal measured from a 4-section pipe, which is labelled as a pristine reference, (b) shows the signal measured from that pipe structure with a joint miss-alignment (tilted joint) at the third section (900 cm). Accordingly, (c), and (d) show signals measured with a corner and a 120 cm diameter manhole at the same location, respectively. The black line indicates the received acoustic signal in the radio-frequency (RF) format. The blue line shows the signal envelope. The red dash line indicates the tape-measured feature positions. The red dots indicates the locations extracted from the acoustic signal using a distance extraction method.

generally small (within 34 cm) enough to be corrected by the high-resolution ultrasonic sensing method in subsequent steps.

Overall, there are four rules summarised for the implementation of acoustic sensing:

i An acoustic echo is generated at the end of the pipe section due to the large acoustic impedance change;
ii The implemented acoustic sensing is designed to filter out aligned joint structures but will indicate miss-aligned joint structures;
iii The applied acoustic wave can propagate around pipe corners to other directions;
iv A manhole structure can generate long acoustic vibration in the time domain. It serves as a point where the robot can be accessed by humans and is therefore considered the endpoint of an autonomous in-pipe inspection.

3.2. Ultrasonic short-range imaging

An ultrasonic pipe imaging algorithm, multi-view pipe total focusing method (Pipe-MTFM), is implemented for both feature characterisation and robotic localisation and navigation. Note that this Pipe-MTFM is modified for in-pipe inspections based on the previous multi-view TFM method [48, 49].

Fig.4 shows six example 3-dimensional (3D) ultrasonic images generated by the hollow-circular array with the Pipe-MTFM imaging algorithm, which can be mathematically expressed as,

$$U^i(\mathbf{p}) = \left| \sum_{T,R} u_{TR}[\tau^i_{TR}(\mathbf{p})] \right|, \tag{1}$$

where $U^i(\mathbf{p})$ is the image intensity of the pixel $\mathbf{p}$, a position vector referred in the Cartesian coordinate, of a 3D Pipe-MTFM image in the ith view, which will be discussed in later sections. u_{TR} are the filtered analytic FMC signals. Subscripts T and R denote the transmitter and the receiver element. $\tau^i_{TR}(\mathbf{p})$ is the time delay in the ith view, which is related to the ray path from the transmitter T to the image pixel ($\mathbf{p}$) and reflected or scattered to the receiver R.

Due to constraints in array design, including the limited element count and geometry arrangement flexibility, ultrasonic imaging using a single view produces large imaging artifacts. Therefore, multiple ultrasonic views are implemented, as the complementary information from each view contributes to enhancing the final image quality. There are three types of ultrasonic transmitting and receiving (TR) ray paths (i.e. imaging views i) currently considered in the Pipe-MTFM imaging algorithm, the direct, halfship, and fullskip ray paths. These ray paths consist of non-skip ray (blue line) and skip ray (black line), as illustrated in Fig.4(a). The reflection point of a skip ray is determined using Fermat's Principle of Least Time for a given pixel coordinate (marked as grey dot). Specifically, the direct ray path is composed of non-skip rays for both the transmitting and receiving paths. The half-skip ray path combines a non-skip ray and a skip ray for the transmitting and receiving paths, respectively, while the full-skip ray path includes two skip rays for both transmitting and receiving paths.

Tippet's fusion approach, is used to combine images generated from the three ray paths into one single view [50, 51]. This process can be expressed as,

$$U_{ti} = \max_i \frac{U^i}{\hat{\sigma}^i_u}, \tag{2}$$

where U_{ti} denotes the fused Pipe-MTFM image by Tippet's data fusion method. $\hat{\sigma}^i_u$ denotes the typical noise pre-measured from pristine pipe structures. It is the maximum likelihood estimator (MLE) of a Rayleigh distribution fitted from a set of pristine pipe images (100 images used in this paper).

For the convenience of structural analysis and object profiling, the fused Pipe-MTFM image, $U_{ti}(\mathbf{p})$, is binarised by an image intensity threshold,

$$B_{ti}(\mathbf{p}) = \begin{cases} 1, & \text{if } [U_{ti}(\mathbf{p})/U_n] \geq U_r, \\ 0, & \text{otherwise}, \end{cases} \tag{3}$$

where $B_{ti}(\mathbf{p})$ is the binarised image intensity at pixel $\mathbf{p}$ fused by Tippet's method. U_n is the reference intensity for the image normalisation process, which is the maximum intensity measured from a plate reflector at 50 cm in open-air. U_r is the intensity threshold in the decibel scale for image binarisation. A single threshold for ultrasonic image binarisation is unreliable for feature characterisation based on imaging, as the ultrasonic image intensity varies with the feature, the distance and the ultrasonic ray path. Hence, a variable ultrasonic image binarisation process is used to generate ultrasonic binary images by a changeable threshold, which is varied in steps, from -10 dB to -25 dB. The system implementation of this dynamic ultrasonic image binarisation process is described in Section 5.

Fig.4 show a set of examples of Tippet's fused Pipe-MTFM binary images. Fig.4(a) shows an empty pipe section at -25 dB. Accordingly, Fig.4(b) to (f) show an irregular wood stack blockage sample (b), a clay wedge sample (c), an aligned pipe joint (d), a tilted pipe joint (e), and a 90° pipe junction (f), respectively. Note

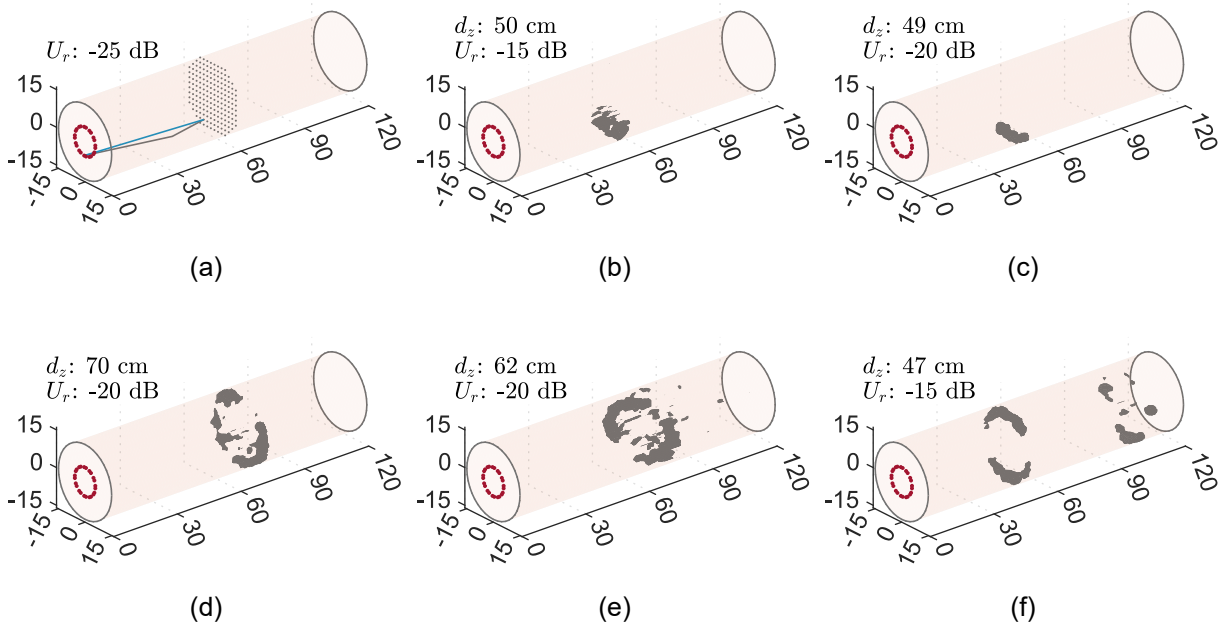

Figure 4: Examples of Tippet's fused multi-view pipe TFM images, (a) an empty pipe section with schematically drawn direct (blue line) and skip (black line) rays and pixel markers, (b) a wood stack blockage sample, (c) a clay wedge blockage sample, (d) an aligned joint, (e) a tilted joint, and (f) a junction, which has two joints separated by appropriately 50 cm.

that photos of these samples used in the experiment are shown in the supplementary information, Section S4. It can be found that the threshold for image binarisation varies with respect to the feature type and distance. Also, for blockage-type features, such as the wood stack and the clay wedge, the non-zero image pixels are clustered in the XY-plane (i.e. the cross-section plane) of the pipe imaging area. While, for pipe-structural features, the high intensity pixels tends to be located uniformly around the pipe boundary. This phenomenon is related to the physical shape of the features, and is used in later sections for feature classification.

4. Ultrasonic image classification

4.1. Pipe-MTFM image processing

The example Pipe-MTFM images shown in Fig.4 are 3D cylindrical binary images (B_{ti}). To enable robotic control with low computational power, these images must be further simplified into parametric information. Here, a Radon Pipe Transform (RPT) is used to simplify the data as illustrated in Fig.S4 (Section S5). From the RPT, three characterisation parameters, are defined: the axial distance (d_z), the axial spread (N_z) and the angular non-zero ratio (r_{nz}), of the imaged feature are obtained from the RPT spectra. d_z in centimetres (cm) indicates axial location of the feature. N_z in pixels (px) indicates the axial length of the feature. r_{nz} indicates the angular non-zero ratio (no unit), which describes the radial uniformity of the pixels. The mathematical expression of r_{nz} is written as,

$$r_{nz} = \frac{1}{N_\phi} \sum_{i=1}^{N_\phi} \left[\begin{cases} 1 \text{ if } : f(\phi_i) \neq 0 \\ 0 \text{ if } : f(\phi_i) = 0 \end{cases} \right] \tag{4}$$

where $f(\phi)$ denotes the angular spectrum from the RPT. N_ϕ is the total number of angles in the RPT. The reason for using r_{nz} is that this parameter is sensitive to the angular change in the XY-plane (the cross-sectional plane) of the Pipe-MTFM image. Collectively, these metrics can be used to classify blockage-type features from structure-type features, as discussed in Fig.4.

4.2. Parametric Relationships

Fig.5 shows the relationships of the three proposed parameters, d_z, N_z, and r_{nz}. Fig.5(a) shows the relationship of the axial distance (d_z) and the angular ratio (r_{nz}). It can be seen that r_{nz} is sensitive to the difference between a blockage and a pipe structure (including aligned and tilted structures), which agrees with the previous

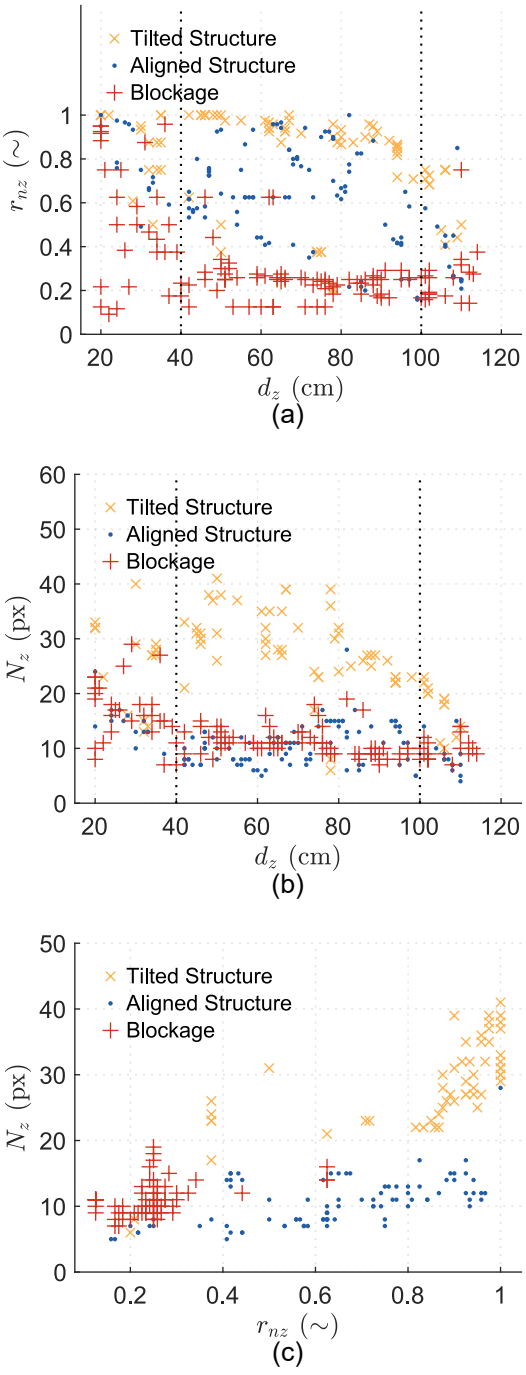

Figure 5: The relationships among d_z, N_z, and r_{nz} with respect to three typical pipe features of sewer pipes, aligned structure, tilted structure, and blockage. (a) shows the relationship between d_z and r_{nz}. Accordingly, (b) shows the relationship between d_z and N_z, and (c) shows the relationship between r_{nz} and N_z. Note that 330 measurements in total were used in this plot measured from five types of features, which include a wood stack, a clay wedge, an aligned joint, a aligned 90° junction (as two aligned joints separated by 50 cm), and a tilted joint, in various distances.

discussion. It is also worth noting that r_{nz} shows better blockage separation capability from 40 cm to 100 cm in the axial direction. This optimal inspection region is due to the element geometry design of the implemented ultrasonic array. A blockage appears as a pipe structure in a Pipe-MTFM image when the feature is close to the array (< 40 cm), which generates inaccuracy when using r_{nz} to distinguish blockage-type features.

Fig.5(b) shows the relationship of d_z and N_z. It can be seen that the tilted structure feature is sensitive to the N_z parameter, as the imaging profile of a tilted structure tends to spread out along the axial direction (Z-axis) compared to those imaging profiles of aligned structures and blockages. N_z also shows a correlation to d_z, which indicates an optimal distance range from 40 cm to 100 cm where the tilted structure is more separable from aligned structure and blockage features by N_z. Hence, an axial distance limit for ultrasonic imaging inspection should be set in the robotic motion control.

Fig.5(c) shows the relationship of r_{nz} and N_z. Note that, data with d_z smaller than 40 cm or larger than 100 cm are filtered out from this plot. It can be seen that the three types of features are separated and clustered using both r_{nz} and N_z. Hence, using these parameters feature classification, specifically for the aligned structure, tilted structure, and blockage, can be implemented into the robotic logic control. Note that, the k-means classifier (KNN) is used here to set up boundaries and classify features based on the proposed parametric study by a supervised learning approach.

5. Autonomous sensing logic

As discussed, the implemented low-frequency acoustic method offers advantages in long-range sensing and signal simplicity for robotic applications, while the proposed high-frequency ultrasonic method shows advantages in high-resolution characterisation, feature classification and also signal simplicity for in-pipe inspections. This paper develops an autonomous in-pipe sensing approach based on a dual-resolution acoustic strategy, integrating low-frequency acoustic waves with high-frequency ultrasonic waves for sewer pipe inspections.

5.1. Sensing range assessment

As the inspection range of the acoustic and ultrasonic sensing are different, a distance calibration is conducted to characterise the optimal sensing region of those two sensing methods.

An experiment was designed to measure the distance-dependent SNR, where setup is schematically shown in

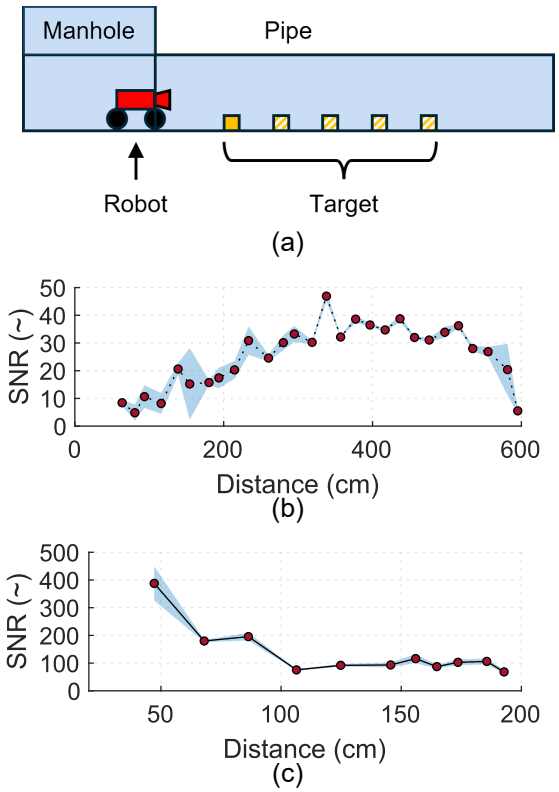

Figure 6: Sensing range calibration of the acoustic and the ultrasonic sensing methods, (a) schematically shows the experimental setup for the distance-dependent SNR calibration, (b) shows the acoustic SNR variation along the axial distance, and (c) shows the ultrasonic SNR variation along the axial distance. Note that this calibration was conducted 10× to evaluate the SNR repeatability, stable SNR calibrations are shown in the range from 200 cm to 540 cm, in which range the SNR standard deviation values are ≤ 5.

Fig.6(a). The robot was placed in a manhole, which is connected at to a pipe section with a total length of 600 cm. A 3D-printed low-level blockage with a height of 4.5 cm (10% blockage) was used as a reference feature for the distance-dependent SNR calibration. The feature position was varied from 60 cm to 600 cm in increments of 20 cm for the acoustic sensing calibration, and 60 cm to 200 cm with the same increment for the ultrasonic sensing calibration. The signals measured from this experiment were then used to calculate the SNR as,

$$SNR(d) = \frac{A(d)}{\sigma(d)} \tag{5}$$

where $A(d)$ here denotes the maximum amplitude of an acoustic signal or maximum intensity of an ultrasonic image at distance d. $\sigma(d)$ denotes the typical noise level which is pre-measured from a pristine pipe setup.

It can be seen from Fig.6(b) that the SNR of acoustic sensing increases when the reference feature is between 60 cm and 240 cm away. This is because there is acoustic crosstalk at the start (time zero) generated by both the excitation vibration from the speaker and the acoustic oscillation in the manhole. The SNR value of acoustic sensing then stabilises between 240 cm and 540 cm. The SNR value then decreases at longer distances. This SNR decrease is due to the pipe length limit (600 cm) of the experimental setup. From Fig.3(a), an acoustic echo is generated at the pipe end due to the impedance difference, which causes the SNR reduction near to the pipe end.

Fig.6(c) shows the calibrated distance-dependent SNR for the ultrasonic imaging device. It can be seen that the SNR value peaks at the start when the reference feature is close to the robot. It then decreases with distance reaching a plateau at 100 cm. Regarding the previous ultrasonic imaging distance results shown in Fig.5, the sensing range for ultrasonic imaging is set from 20 cm to 120 cm to avoid the dead-zone area of the array at time zero and maintain high resolution imaging coverage. For feature characterisation, a subset range of 40 cm to 100 cm in the images is used, following the results shown in Fig.5.

5.2. Sensing logic for robot motion control

According to the acoustic sensing results shown in Fig.3 and the sensing range calibration in Fig.6, it can be seen that acoustic sensing is good for long-range coverage but limited in its accuracy, which generates errors for feature localisation. Ultrasonic imaging using a transducer array has much shorter wavelength and hence has the potential for much greater characterisation performance, albeit over a shorter range [52].

Hereby, robot moving steps, d_{ia} can be obtained based on the feature distances, d_a, from the acoustic sensing. d_{iu} is the corrected moving step based on ultrasound to correct uncertainty in position. Details of the d_{ia} and d_{iu} calculations are shown in Section S3.2. d_{uc} denotes the position adjustment within each moving step according to ultrasonic sensing for better feature inspection, i.e. to control the distance between the array and a feature between 40 cm to 100 cm. Distance data from motor encoders shows large errors (in Section S7) and is not used in the current paper.

Based on the discussions above, an autonomous sensing logic is developed using both the acoustic and the ultrasonic methods for pipe inspections, as shown in Fig.7. As the acoustic sensing is suitable for long-range feature scoping, the process is started by acoustic sensing to determine potential features inside the pipe potentially up to the next manhole, which can be identified from the received acoustic signal by its high amplitude and long-duration echo. Locations of the potential features can then be extracted from the acoustic signal and the robot will drive down to those features one by one for detailed characterisation with ultrasonic imaging. At each location, a Pipe-MTFM image is generated from the ultrasonic sensing.

Ultrasonic image binarisation is then performed to analyse the feature profile according to the image threshold, U_r. The system evaluates whether the number of pixels (N_p) exceeding the threshold is sufficient ($N_p > 125$). This reference value is determined by the robot's chassis height (4 cm) and pixel size (0.8 cm), ensuring any potential blockage feature bigger than the robot (i.e. occupying a pixel volume of $5 \times 5 \times 5$) can be detected at the given threshold. If the pixel count above U_r is insufficient, the system decreases the threshold by 5 dB and repeats the binarisation process. If the pixel count remain below the threshold even at -25 dB, the system identifies the current pipe section as empty and proceeds to the next d_{ia}. If the pixel count exceeds the threshold, the binarised ultrasonic image will pass to the next stage for feature characterisation and classification, following the RPT characterisation procedures.

Based on the characterisation results, the system will determine whether the distance between the robot and the feature is within an appropriate distance range (40 cm to 100 cm) to decide whether to apply a position adjustment, d_{uc} for better ultrasonic imaging inspection. If this position adjustment is unnecessary, the system will then evaluate whether the feature is a structure-type object or a blockage-type object. If it is a potential blockage, the system will drive the robot back to the start. If the feature is classed as a structure, the system will then

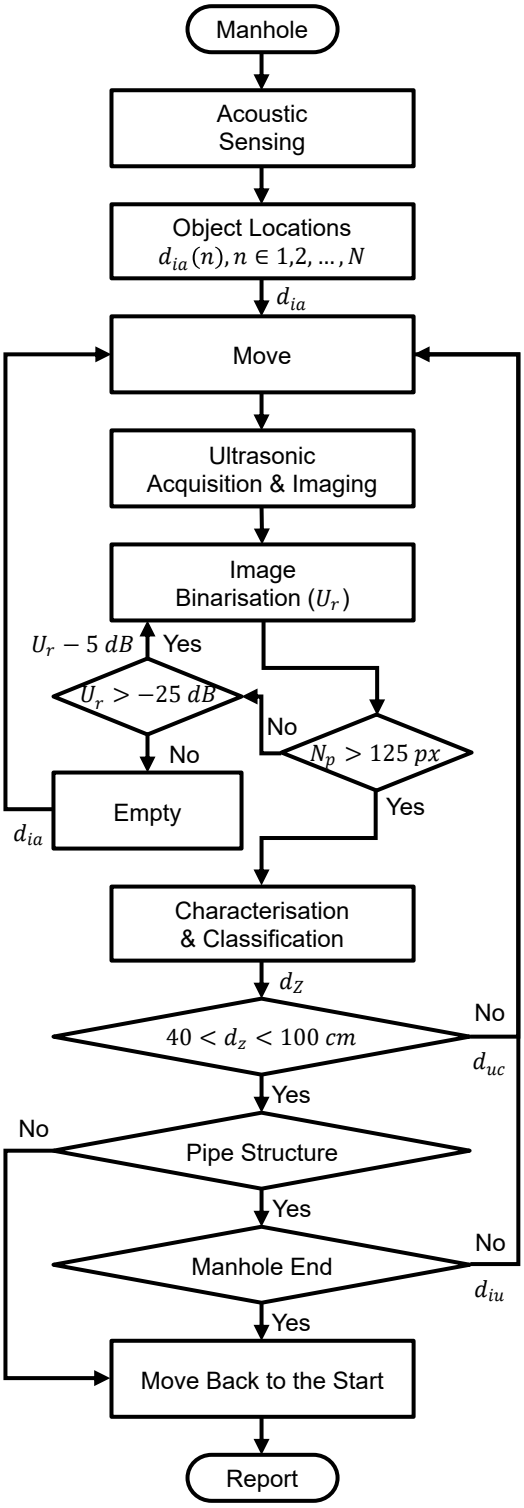

Figure 7: Diagrams of the autonomous sensing and robot positioning logic for pipe inspection by the combination of acoustic and ultrasonic sensing techniques.

consider whether this feature is the manhole (i.e. pipe end) location acquired from the acoustic sensing. If it is the manhole, the system will also drive the robot back to the start and report this. If not, the system will then drive the robot to the next inspection point according to the acoustic sensing result.

6. Autonomous pipe inspection

6.1. Experimental pipe setup

Fig.8 illustrates the experimental setup built to validate the autonomous pipe inspection approach. The setup incorporates six pipe sections, a 90° junction, a 120 cm lateral section, and a manhole. The total length of the setup is approximately 1800 cm, with the inspection starting position marked by a red arrow on the far right of the pipe network. From the starting position, the first three pipe sections were rubber-sealed and precisely aligned, these are good pipe structures and acoustically invisible. A 120 cm pipe lateral and a 90° junction were positioned at the end of the fourth section. A tilted joint was placed at the end of the fifth section, and a manhole (i.e., the pipe end) was located at the end of the setup. Consequently, there are four detectable features in this setup for acoustic sensing: the start of the junction (1130 cm), the end of the lateral (1250 cm), the tilted pipe joint (1500 cm), and the pipe end manhole (1800 cm). Photos of those acoustically detectable features are shown in Fig.S5 (Section S6). Overall, there are 7 features in total in the experimental setup. The first 3 pipe joint features are good structures which are undetectable by acoustic sensing. The following 4 features are designed to be detectable and marked by numbered red arrows in Fig.8.

6.2. Autonomous inspection results

Following the autonomous sensing and positioning logic outlined in Fig.7, a total of 30 inspection trials were conducted without any human intervention. Each trial begins with the robot positioned at the starting manhole, it then proceeds to inspect the entire pipe system, following the proposed sensing and positioning logic until reaching its endpoint. Fig.9 shows results obtained from one example run, which starts with the capture of an acoustic signal shown in Fig.9(a). It can be seen that the echo generated by the pipe end manhole, noted as (4), at 1800 cm is the largest echo whose amplitude is used as the reference to extract the distance information for other acoustically detectable features. Echoes, noted as (1), (2), and (3) are generated by the 90° junction, the end of the pipe lateral, and the tilted joint features, respectively. Corresponding ultrasonic Pipe-MTFM images are shown in the figure with the same numbering. Fig.9(1) and (4) clearly show the aligned joint structure of the pipe junction and the pipe end manhole. In terms of the tilted joint, it looks like a blockage in Fig.9(3), which is due to the view angle of the 3D image.

Fig.9(2) indicates that there is no feature in the main pipes at the echo (2) location shown in the acoustic result. This is because the acoustic wave can propagate into the pipe laterals, and generate backscattered echoes at the features inside along the pipe lateral. These echoes appear in the acoustic signal which cause artifacts for acoustic sensing in the main pipe. Hence, ultrasonic imaging can be used to distinguish the acoustic echoes generated in pipe laterals. If the ultrasonic imaging result shows an empty pipe section at a location reported by the acoustic sensing, it can then confirm that the acoustic echo is generated from propagation within pipe laterals, rather than the main pipe.

Repeatability analysis is performed based on the inspection results from the 30 inspection trials. Fig.10 shows the results of the repeatability analysis. Fig.10(a) shows the repeatability analysis of the sensing localisation performance for detectable features. Feature locations of the junction (1), the tilted joint (3), and the pipe end manhole feature (4) are distance values obtained from the dual-resolution acoustic sensing. The location of the lateral end (2) is only calculated based on the acoustic sensing results as this feature is inside the pipe lateral, rather than the main pipe. Hence this feature cannot be detected by the ultrasonic imaging. The variation in feature localisation is minimal relative to the scale of the pipe network. The average standard deviation for feature localisation at the pipe junction (1), lateral end (2), and pipe end manhole (4) is 8.0 cm, with the highest standard deviation of 9.6 cm observed at the pipe end manhole (4) in a pipe system with a total length of 1800 cm. The maximum localisation error recorded is 25 cm, occurring at the pipe end manhole (4). Note that there is one outlier shows in Fig.10(a) for the tilted joint (3) localisation. This outlier is generated due to the large error from the acoustic sensing which exceeds the correction range of the ultrasonic sensing (currently limited to 120 cm in the experiment). This error can be solved by increasing the detection range of the ultrasonic imaging.

Fig.10(b) shows the repeatability analysis on the ultrasonic image classification. It is worth noting that, as mentioned in Section 4, features that are classified in this work are empty pipe (EP), blockage (B), aligned structure (AS, including aligned pipe joint, junction and

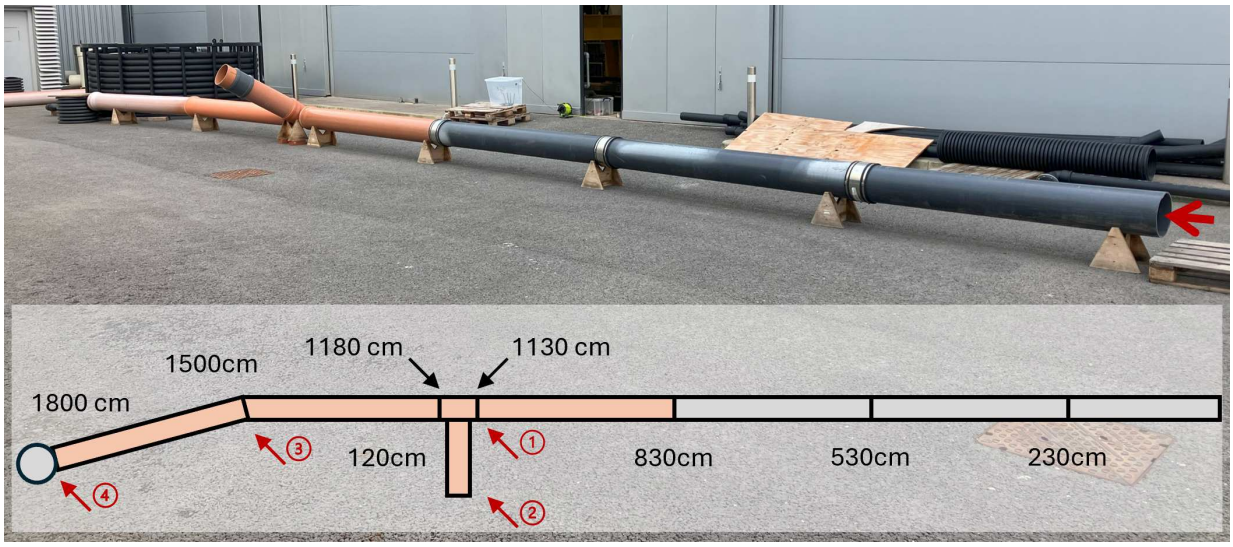

Figure 8: Photo of the pipe setup used for the autonomous inspection experiment. The starting position of the inspection is marked by a red arrow in the photo. A schematic at the bottom illustrates the locations of all designed features in the setup. Four key features to be characterised during the inspection are indicated by numbered red arrows: (1) the pipe junction, (2) the lateral end, (3) the tilted pipe joint, and (4) the pipe end manhole. All pipe joints of these black pipes are rubber-sealed and precisely aligned, and the pipe sections and fittings used in this setup are certified to the BS EN 1401-1 standard.

end manhole), and tilted structure (TS, including tilted pipe joint, junction, and end manhole). Based on the designed pipe network shown in Fig.8, classification result should report 'AS' at the pipe junction feature (1), 'EP' at the lateral end location (2), 'TS' at the tilted pipe joint feature (3). and 'TS' at the pipe end manhole feature (4). Due to space constraints in the experimental area, a gap exists between the manhole and the pipe end, as illustrated in Fig.S5. This gap causes the robot to report 'TS' when capturing the manhole gap and 'AS' when detecting only the pipe end.

Fig.10(b) shows the classification results grouped according to the actual pipe features. In general, there should be 4 detected features in each inspection trial, which yields a total detection number of 120 for 30 inspection trials. However, due to the short pipe lateral length and the instability of acoustic sensing, the lateral end feature is missed occasionally during the inspection. Hence, the total feature detection number is 106 across the 30 trials. There are 13 missing reports for the lateral end feature and 1 missing report for the pipe end manhole feature.

Fig.10(b) and (c) are combined to show the feature classification accuracy of the developed robot system. It can be seen that a 100% accuracy is shown for the first pipe junction feature (1). While, it is only 53% for the lateral end feature (2) as there are 13 'missing' reports. The classification accuracy is 94% if the missing count is excluded, as it shown in Fig.10(c). The classification accuracy of the tilted pipe joint feature (3) is 77% (23) from the 30 inspection trials. The tilted joint occasionally looks like an aligned joint when the ultrasonic image is binarised (as illustrated in Fig.S3(g)). This caused the error report in the feature classification and can be improved by tuning the decibel range for plotting. Also, the 'EP' report at the tilted pipe joint is due to the large distance error from the acoustic sensing exceeded the compensation range using ultrasonic imaging. This large distance error makes the robot stop at an empty section and causes the 'EP' report at the tilted pipe joint feature. This error can be improved by increasing the ultrasonic sensing range, as it is currently limited to 120 cm. For the pipe end manhole feature (4), the classification accuracy is 73% (22 'TS' report) out of the 30 trials. The overall classification accuracy of both feature 3 and 4 is 76% as shown in Fig.10(c). The 'AS' reports (10 in total) are due to the overlapped ultrasonic amplitudes of 'AS' and 'TS' classes, and hence that cannot always be correctly classified, as shown in Fig.S3(i). There is one report that the pipe end manhole is recognised as a blockage 'B'. This is due to the inconsistent ultrasonic responses at the pipe end and the image of this report is shown in Fig.S3(h).

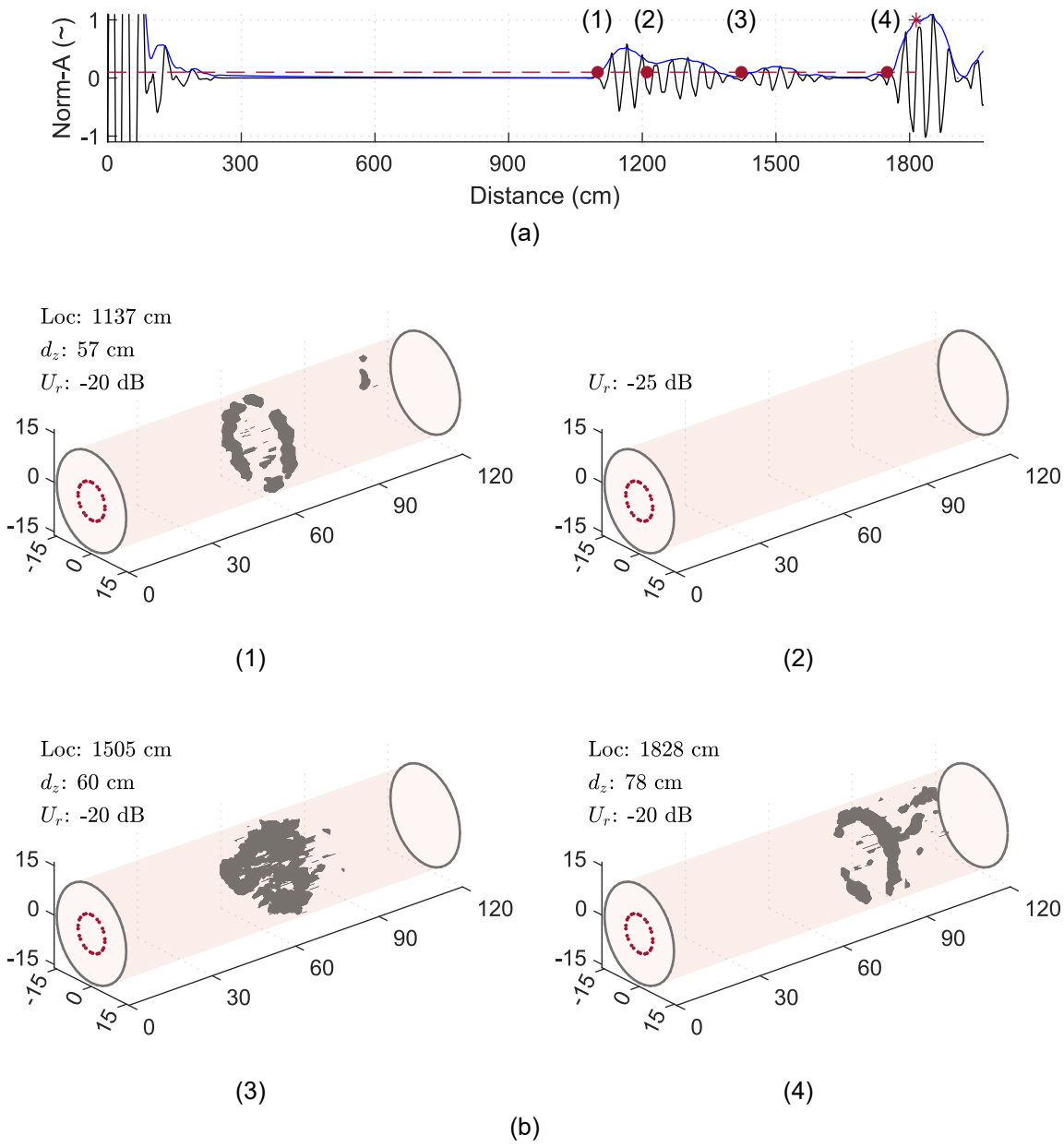

Figure 9: Acoustic and ultrasonic sensing results from the autonomous pipe inspection experiment, (a) is the acoustic signal acquired from the pipe network setup, (b) show the ultrasonic images captured at the acoustic echoes shown in (a), corresponding to the feature numbering shown in Fig.8, respectively the start joint of the 90° junction (1), the acoustic artifacts generated by the lateral end (2), the tilted pipe joint (3), and the pipe end manhole (4), respectively.

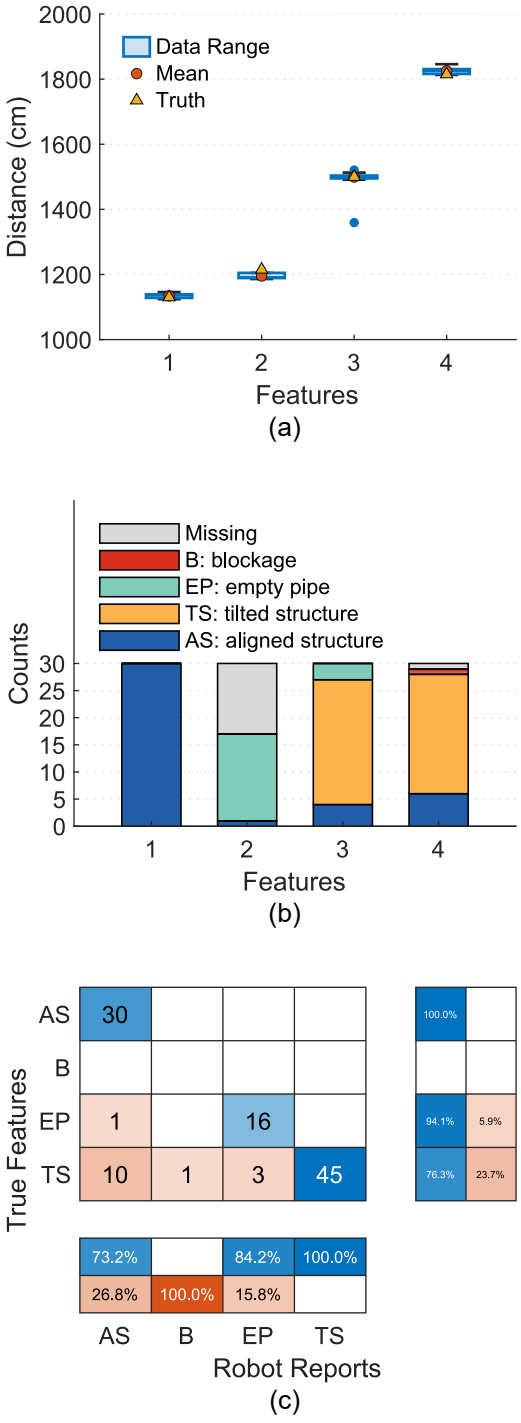

Figure 10: Autonomous inspection by the dual-resolution acoustic sensing measure, (a) shows the repeatability plot of the detected location of those pipe features, (b) shows the repeatability analysis of the feature classification based on ultrasonic imaging results, and (c) shows the confusion matrix of the robot reports. Note that feature 1 should be 'AS', feature 2 should be 'EP', and feature 3 and 4 should be 'TS', due to the miss-aligned manhole setup shown in Fig.S5.

7. Conclusions

This paper demonstrated a robotic apparatus developed for autonomous pipe inspection, using a dual-resolution acoustic sensing measure. The robot was equipped with a low-frequency (300 Hz to 600 Hz) acoustic sensing system for long-range, coarse identification of potential features within pipes. Additionally, a short-range, air-coupled ultrasonic imaging system was incorporated, leveraging the Pipe-MTFM ultrasonic imaging algorithm for high-resolution feature characterisation. This integrated dual-resolution acoustic sensing approach allows the robotic apparatus to perform autonomous inspections within a controlled laboratory pipe network.

Thirty autonomous inspection trials were conducted within a specially designed pipe network spanning 1800 cm. Four artificial features were strategically placed within this network for evaluation. The combined use of acoustic and ultrasonic sensing yielded good feature localisation accuracy, with a maximum error of 25 cm observed at the pipe end manhole feature across all trials. Additionally, the inspections demonstrated good repeatability, with an average standard deviation of 8 cm noted across all four features. Given the scale of the pipe network, these errors are relatively small, affirming the accuracy of the proposed sensing combination for feature localisation in autonomous inspection experiments. Moreover, there are total 106 feature detections reported by the robot after 30 inspection trials, which should have 120 feature detections according to the pipe setup. This feature missing error is because the neighbouring features are too close for the acoustic sensing, which means one of the features can only be detected occasionally.

In terms of feature classification accuracy, the proposed robotic apparatus achieved rates of 100%, 53% (94% excluding the acoustic missing error), 77%, and 73% for the pipe junction (1), the lateral end (2), the tilted pipe joint (3), and the pipe end manhole (4), respectively. The classification accuracy is constrained by limitations in both the acoustic sensing and ultrasonic imaging processes. Acoustic sensing occasionally fails to detect a feature when two features are situated close to each other. Moreover, the ultrasonic imaging results can vary for the same feature depending on the thresholds set for image binarisation, leading to inconsistencies in feature classification based on the three parameters, d_z, N_z, and r_{nz}. However, it is important to note that, for the pipe setup used in the experiment, the proposed dual-resolution acoustic sensing method successfully detects all designed failure structures without any

missing reports.

Based on the findings of this study, future improvements can focus on three parts. Firstly, improving the image binarisation process for ultrasonic imaging may improve the precision of image-based classification. Secondly, expanding the feature classification process to involve a broader range of feature types would enable more precise robotic control during autonomous in-pipe inspections. Finally, conducting additional trials in real-world pipe systems will be essential for validating the proposed autonomous inspection approaches.

8. Acknowledgements

The authors are grateful to the UK's Engineering and Physical Sciences Research Council (EPSRC Grant EP/S016813/1) for support of this work. The authors are also grateful to their industry partners for their advice about the commercial systems for the inspection of buried pipes.

References

[1] J. M. Mirats Tur, W. Garthwaite, Robotic devices for water main in-pipe inspection: A survey, Journal of Field Robotics 27 (4) (2010) 491–508.

[2] J. B. Haurum, T. B. Moeslund, A survey on image-based automation of cctv and sset sewer inspections, Automation in Construction 111 (2020) 103061.

[3] R. Qi, M. Cao, D. Yntema, Recent developments of subsurface small-leak detection techniques in water distribution networks: a review, IEEE Robotics & Automation Magazine.

[4] O. A. INFRASTRUCTURE, A comprehensive assessment of America's infrastructure, in: A comprehensive assessment of America's infrastructure, ASCE, ASCE, 2021, pp. 1–111.

[5] A. Negm, X. Ma, G. Aggidis, Review of leakage detection in water distribution networks, in: IOP conference series: earth and environmental science, Vol. 1136, IOP Publishing, 2023, p. 012052.

[6] D. Huang, X. Liu, S. Jiang, H. Wang, J. Wang, Y. Zhang, Current state and future perspectives of sewer networks in urban china, Frontiers of Environmental Science & Engineering 12 (2018) 1–16.

[7] K. F. Makris, J. Langeveld, F. H. Clemens, A review on the durability of pvc sewer pipes: research vs. practice, Structure and Infrastructure Engineering 16 (6) (2020) 880–897.

[8] J. Yang, T. Zayed, D. Arimiyaw, R. Xiao, A comprehensive review of influential factors and predictive techniques of time to failure for sewer pipes, Tunnelling and Underground Space Technology 157 (2025) 106357.

[9] R. Wirahadikusumah, D. M. Abraham, T. Iseley, R. K. Prasanth, Assessment technologies for sewer system rehabilitation, Automation in Construction 7 (4) (1998) 259–270.

[10] I. C. Scheperboer, R. A. Luimes, A. S. Suiker, E. Bosco, F. Clemens, Experimental-numerical study on the structural failure of concrete sewer pipes, Tunnelling and Underground Space Technology 116 (2021) 104075.

[11] S. Foorginezhad, M. Mohseni-Dargah, K. Firoozirad, V. Aryai, A. Razmjou, R. Abbassi, V. Garaniya, A. Beheshti, M. Asadnia, Recent advances in sensing and assessment of corrosion in sewage pipelines, Process Safety and Environmental Protection 147 (2021) 192–213.

[12] M. Wang, H. Luo, J. C. Cheng, Towards an automated condition assessment framework of underground sewer pipes based on closed-circuit television (cctv) images, Tunnelling and Underground Space Technology 110 (2021) 103840.

[13] K. Wu, A survey on wireless in-pipe inspection robotics, International Journal of Intelligent Robotics and Applications (2024) 1–23.

[14] C. Parrott, T. J. Dodd, J. Boxall, K. Horoshenkov, Simulation of the behavior of biologically-inspired swarm robots for the autonomous inspection of buried pipes, Tunnelling and Underground Space Technology 101 (2020) 103356.

[15] M. J. Chae, T. Iseley, D. M. Abraham, Computerized sewer pipe condition assessment, in: New Pipeline Technologies, Security, and Safety, American Society of Civil Engineers, 2003, pp. 477–493.

[16] Z. Liu, Y. Kleiner, State of the art review of inspection technologies for condition assessment of water pipes, Measurement 46 (1) (2013) 1–15.

[17] S. N. Betgeri, S. R. Vadyala, J. C. Matthews, M. Madadi, G. Vladeanu, Wastewater pipe condition rating model using k-nearest neighbors, Tunnelling and Underground Space Technology 132 (2023) 104921.

[18] N. Wang, D. Ma, X. Du, B. Li, D. Di, G. Pang, Y. Duan, An automatic defect classification and segmentation method on three-dimensional point clouds for sewer pipes, Tunnelling and Underground Space Technology 143 (2024) 105480.

[19] C. Yang, F. Zheng, Z. Kapelan, D. Savic, G. Pan, Y. Feng, Y. Ma, Automated quantification of sewage pipe cracks using deep learning for urban water environment management, Tunnelling and Underground Space Technology 155 (2025) 106195.

[20] Q. Ma, G. Tian, Y. Zeng, R. Li, H. Song, Z. Wang, B. Gao, K. Zeng, Pipeline in-line inspection method, instrumentation and data management, Sensors 21 (11) (2021) 3862.

[21] J. B. Nestleroth, R. J. Davis, Application of eddy currents induced by permanent magnets for pipeline inspection, NDT & E International 40 (1) (2007) 77–84.

[22] H. Huang, N. Sakurai, T. Takagi, T. Uchimoto, Design of an eddy-current array probe for crack sizing in steam generator tubes, NDT & E International 36 (7) (2003) 515–522.

[23] Y. He, G. Tian, M. Pan, D. Chen, Non-destructive testing of low-energy impact in cfrp laminates and interior defects in honeycomb sandwich using scanning pulsed eddy current, Composites Part B: Engineering 59 (2014) 196–203.

[24] H. Q. Pham, B. V. Tran, D. T. Doan, Q. N. Pham, K. Kim, C. Kim, F. Terki, Q. H. Tran, et al., Highly sensitive planar hall magnetoresistive sensor for magnetic flux leakage pipeline inspection, IEEE Transactions on Magnetics 54 (6) (2018) 1–5.

[25] Y. Yu, A. Safari, X. Niu, B. Drinkwater, K. V. Horoshenkov, Acoustic and ultrasonic techniques for defect detection and condition monitoring in water and sewerage pipes: A review, Applied Acoustics 183 (2021) 108282.

[26] R. Fletcher, M. Chandrasekaran, Smartball™: a new approach in pipeline leak detection, in: International Pipeline Conference, Vol. 48586, 2008, pp. 117–133.

[27] F. Kirchner, J. Hertzberg, A prototype study of an autonomous robot platform for sewerage system maintenance, Autonomous robots 4 (4) (1997) 319–331.

[28] E. Rome, J. Hertzberg, F. Kirchner, U. Licht, T. Christaller, Towards autonomous sewer robots: the makro project, Urban Water 1 (1) (1999) 57–70.

[29] H. Hussein, A. A. Ramadan, R. K. Gupta, Telerobot: Failure detection using imaging technique for piping internal surfaces, in: IOP Conference Series: Materials Science and Engineering, Vol. 943, IOP Publishing, 2020, p. 012020.

[30] M. Bubanja, M. M. Markus, M. Djukanovic, M. Vujovic, Robot for cleaning ventilation ducts, in: New Technologies, Development and Application 4, Springer, 2019, pp. 180–190.

[31] D. V.-K. Le, Z. Chen, R. Rajkumar, Multi-sensors in-line inspection robot for pipe flaws detection, IET Science, Measurement & Technology 14 (1) (2020) 71–82.

[32] A. Burguera, G. Oliver, J. D. Tardos, Robust scan matching localization using ultrasonic range finders, in: 2005 IEEE/RSJ International Conference on Intelligent Robots and Systems, IEEE, 2005, pp. 1367–1372.

[33] H.-J. Zhong, Z.-W. Ling, C.-J. Miao, W.-C. Guo, P. Tang, A new robot-based system for in-pipe ultrasonic inspection of pressure pipelines, in: 2017 Far East NDT New Technology & Application Forum (FENDT), IEEE, 2017, pp. 246–250.

[34] R. K. Rachev, P. D. Wilcox, A. Velichko, K. McAughey, J. Giese, Ultrasonic immersion testing for crack detection and depth sizing in large diameter pipes, in: Proc. ECNDT, 2018, pp. 1–8.

[35] L. Le Jeune, S. Robert, E. L. Villaverde, C. Prada, Plane wave imaging for ultrasonic non-destructive testing: Generalization to multimodal imaging, Ultrasonics 64 (2016) 128–138.

[36] C. Holmes, B. W. Drinkwater, P. D. Wilcox, Post-processing of the full matrix of ultrasonic transmit–receive array data for non-destructive evaluation, NDT & E International 38 (8) (2005) 701–711.

[37] R. K. Vithanage, E. Mohseni, Z. Qiu, C. MacLeod, Y. Javadi, N. Sweeney, G. Pierce, A. Gachagan, A phased array ultrasound roller probe for automated in-process/interpass inspection of multipass welds, IEEE Transactions on Industrial Electronics 68 (12) (2020) 12781–12790.

[38] Y. Yu, R. Worley, S. Anderson, K. V. Horoshenkov, Microphone array analysis for simultaneous condition detection, localization, and classification in a pipe, The Journal of the Acoustical Society of America 153 (1) (2023) 367–383.

[39] A. R. K. Towlson, A. J. Croxford, B. W. Drinkwater, Ultrasonic nondestructive characterization of blockages and defects in underground pipes, IEEE Transactions on Ultrasonics, Ferroelectrics, and Frequency Control 69 (8) (2022) 2540–2554. doi:10.1109/TUFFC.2022.3183339.

[40] G. Allevato, J. Hinrichs, M. Rutsch, J. P. Adler, A. Jäger, M. Pesavento, M. Kupnik, Real-time 3-d imaging using an air-coupled ultrasonic phased-array, IEEE Transactions on Ultrasonics, Ferroelectrics, and Frequency Control 68 (3) (2020) 796–806.

[41] G. Allevato, M. Rutsch, J. Hinrichs, C. Haugwitz, R. Müller, M. Pesavento, M. Kupnik, Air-coupled ultrasonic spiral phased array for high-precision beamforming and imaging, IEEE Open Journal of Ultrasonics, Ferroelectrics, and Frequency Control 2 (2022) 40–54.

[42] Y. Yu, K. V. Horoshenkov, S. Tait, Microphone array analysis of the first non-axisymmetric mode for the detection of pipe conditions, The Journal of the Acoustical Society of America 155 (1) (2024) 575–587.

[43] R. Worley, Y. Yu, K. V. Horoshenkov, S. R. Anderson, Acoustic echo sensing for robot localization in buried pipe networks, IEEE Sensors Journal.

[44] X. Sun, A. J. Croxford, B. W. Drinkwater, Multiplexing Array Controller Based on Digilent Analog Discovery 2, `https://doi.org/10.17632/dxy9sb7v4z.1/`, [Deactivated; shared via Mendeley Data and will be activated upon paper publication] (2025).

[45] P. M. Morse, K. U. Ingard, Theoretical acoustics, Princeton university press, 1986.

[46] S. J. Wright, R. D. Nowak, M. A. Figueiredo, Sparse reconstruction by separable approximation, IEEE Transactions on signal processing 57 (7) (2009) 2479–2493.

[47] S. S. Chen, D. L. Donoho, M. A. Saunders, Atomic decomposition by basis pursuit, SIAM review 43 (1) (2001) 129–159.

[48] J. Zhang, B. W. Drinkwater, P. D. Wilcox, A. J. Hunter, Defect detection using ultrasonic arrays: The multi-mode total focusing method, NDT & E International 43 (2) (2010) 123–133.

[49] N. Budyn, A. J. Croxford, R. L. Bevan, J. Zhang, P. D. Wilcox, Characterisation of small embedded two-dimensional defects using multi-view total focusing method imaging algorithm, NDT & E International 119 (2021) 102413.

[50] P. D. Wilcox, A. J. Croxford, N. Budyn, R. L. Bevan, J. Zhang, A. Kashubin, P. Cawley, Fusion of multi-view ultrasonic data for increased detection performance in non-destructive evaluation, Proceedings of the Royal Society A 476 (2243) (2020) 20200086.

[51] R. L. Bevan, N. Budyn, J. Zhang, A. J. Croxford, S. Kitazawa, P. D. Wilcox, Data fusion of multiview ultrasonic imaging for characterization of large defects, IEEE Transactions on Ultrasonics, Ferroelectrics, and Frequency Control 67 (11) (2020) 2387–2401.

[52] A. R. K. Towlson, A. J. Croxford, B. W. Drinkwater, Air-coupled ultrasonic arrays for assessment of pipe internal geometry and surface condition, IEEE Transactions on Ultrasonics, Ferroelectrics, and Frequency Control 71 (4) (2024) 474–484. doi:10.1109/TUFFC.2024.3362904.